Diode laser spectrometer for high-precision measurements

A.I. Nadezhdinskii, Ya.Ya. Ponurovskii

Abstract. **The issues of the development, calibration and putting into operation of a diode laser spectrometer for high-precision measurements are considered. The tests rely on the use of an isolated P20 line of the 00031 – 00001 band of the $^{12}C^{16}O_2$ molecule. The spectrometer error budget is analysed. A software programme for the approximation of a spectral line contour is designed and the procedure is analysed. It is shown that, for a baseline with a relative level of 2.3×10^{-5}, it is optimal to use no more than six fitting parameters in the line contour approximation. The measured integral intensity of the analytical line constitutes $5.3865(85) \times 10^{-23}$ cm per molecule.**

Keywords: diode laser, spectroscopy, spectral line intensity.

1. Introduction

In this paper, we discuss the issues of diode laser (DL) spectroscopy. All the DL components (active medium, pump source, resonator) are contained in a single chip. For the first time, the use of semiconductors as an active medium of a laser, with the p–n transition in lasers used for pumping, was proposed in works [1–3]. It took only 4 years from the proposal to the development of the first DL [4, 5].

In 1964, a new type of diode lasers based on IV–VI (PbTe type) semiconductors was designed, with lasing in the mid-IR range [6]. Using this DL type 50 years ago, Hinckley [7] was the first to record the high-resolution spectrum of the SF_6 molecule. This work marked the beginning of what is now called diode laser spectroscopy (DLS).

An insight into the research covered by DLS can be found in the proceedings of ten International Conferences on Tunable Diode Laser Spectroscopy (TDLS) [8]. Selected papers of these conferences have been published in special issues of journals [9–17]. A number of books and reviews [18–30], as well as proceedings of thematic conferences [31–36], have been dedicated to this topic. The dominant DLS area is analytical applications for which the measurement method sensitivity is of fundamental importance. For its characterisation, the noise equivalent absorbance (NEA) parameter is used. Allan plots [37] are employed to analyse the time evolution of the studied values, which show the value deviation as a function of the averaging time. Figure 1 displays the summary Allan plot of NEA in DLS according to the literature data [38–54].

A.I. Nadezhdinskii, Ya.Ya. Ponurovskii Prokhorov General Physics Institute, Russian Academy of Sciences, ul. Vavilova 38, 119991 Moscow, Russia; e-mail: Ponur1960@yandex.ru
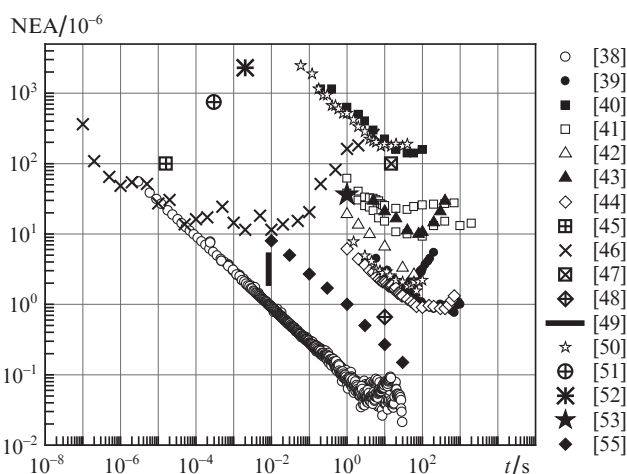
Figure 1. Summary Allan plot of NEA according to the literary data.

It is worth mentioning papers [54, 55], which describe in detail different types of noise in DLS.

In more detail, the dependence of NEA on the averaging time is shown in Fig. 2. Typically, the sensitivity is limited by the baseline drift and flicker noise (see Fig. 2). Flicker noise is not accumulated during averaging, while the baseline drift increases the noise level with increasing averaging time.
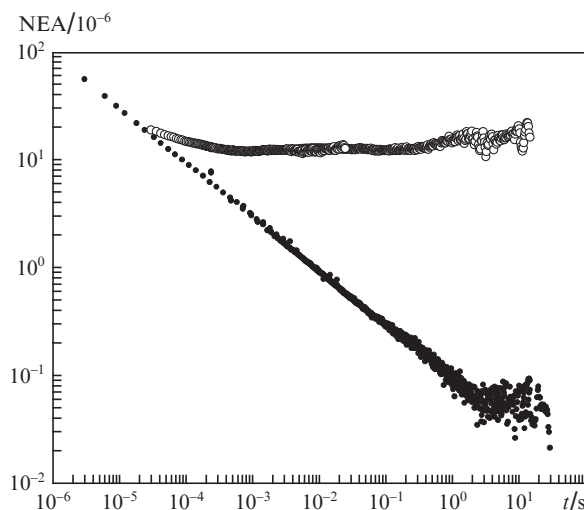

Figure 2. Dependence of NEA on averaging time [38]: in the presence of (○) flicker noise and of (●) baseline drift after noise suppression.

After identifying the physical mechanisms responsible for the formation of flicker noise [56] and baseline drift [57], methods for their suppression were developed. This made it possible to reach the sensitivity limit (see Fig. 2), which is more than an order of magnitude higher than the best results in the world (see comparison in [38] and Fig. 1). This limit is fundamental because it is stipulated by the quantum noise of a diode laser. Poisson noises of photons and electrons in a photodetector and quantum noises of the DL field [38] were also identified. An overview of the results of various analytical applications of DLS, obtained at our Institute, is given in [58].

This paper is dedicated to another direction of DLS, i.e. high-precision DLS, where the accuracy of measurements comes to the fore.

2. Optical scheme of a spectrometer for high-precision DLS

The spectrometer uses a DL with a fibre pigtail. Four Y-shaped fibre splitters form an optical scheme of the spectrometer with five channels, the signals of which are recorded by five photodiodes (PDs) (Fig. 3).
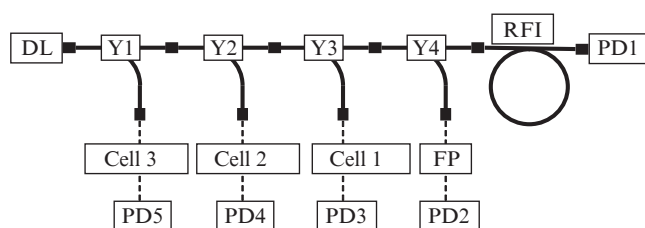

Figure 3. Optical scheme of the spectrometer:
(RFI) ring fibre interferometer; (FP) Fabry–Perot etalon.

These five channels contain three cells (Cell 1, Cell 2, Cell 3), a Fabry–Perot (FP) etalon and a ring fibre interferometer (RFI). Solid lines in Fig. 3 are optical fibres, and dashed lines are axes of the beams propagating in the atmosphere. The axes of the lenses that focus radiation onto PDs are shifted to significant angles from the axes of radiation propagation. This is done to eliminate the interference of radiation reflected from the inner surfaces of the lenses. The spectrometer operation regimes allow the signals from any three photodiodes to be recorded. The changes in the configuration and operation

regimes of the spectrometer are due to the software changes. In this case, there are no changes in the optical system, so that the spectrometer operation is very stable.

Cells 1 and 2 are made of stainless steel, i.e. tubes with a diameter of 40.15 mm with welded flanges. The flanges have grooves with glued glass windows.

To measure the cell lengths, we used metal rulers and a calliper manufactured at OJSC 'Kalibr' (Moscow) and Chelyabinsk Tool Plant (Chelyabinsk), respectively. The ruler error according to GOST 427-75 is 0.2 mm [59], and the calliper error according to GOST 166-89 is 0.05 mm [60].

First, the metres were calibrated. Within their errors, the readings of rulers and calliper coincided. Then, the lengths of cells 1 and 2 were measured, amounting to $L_1 = 183.36(9)$ cm and $L_2 = 183.50(4)$ cm.

Cell 1 is used in the reference channel, where the measurement accuracy requirements are lower than in the analytical channel that uses cell 2.

Measurements are also accompanied by a systematic error associated with the laser beam propagation at an angle to the cell axis, which is necessary to eliminate the interference of beams reflected from the cell windows. Using a collimator, the DL radiation is transformed into a parallel beam and directed to a multipass cell 3 (Herriot system) with a distance between the mirrors' centres of 257.75 mm and the number of passes equal to 59. The optical length here is determined by calculations and amounts to $L_3 = 1517.15(51)$ cm. The length of cell 3 is also determined by measuring the absorption spectra.

3. Diode laser

The spectrometer includes several tens of DLs from different manufacturers (for example, [61–65]), providing the overlap of the spectral range of 5300–7800 cm^{-1}, where the overtones and composite vibrations of many molecules are located. All these DLs have a fibre pigtail.

3.1. Spectrometer frequency scale calibration

Frequency scale calibration in a high-precision DL spectrometer started from the calibration of a Fabry–Perot etalon, which was a cylinder of KU fused silica with a diameter of 30 mm and a length of 69 mm, with antireflection coating at the end faces for the near-IR range. DLS is based on the dependence of the DL radiation frequency on temperature. A special software programme provides a slow DL tempera-
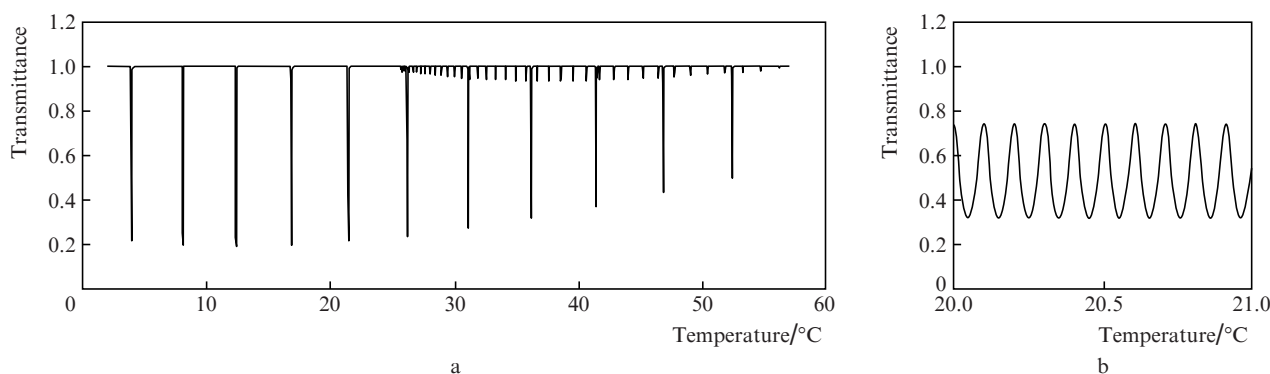

Figure 4. Transmission spectra of (a) the CO_2 and (b) FP molecules.

ture change from 2 °C to 56 °C. This scan takes about 25 min. A change in temperature leads to a change in the radiation frequency of a particular DL (in this case, NEL SN922076) from 6963 to 6937 cm^{-1}. In this case, the transmission spectra of CO_2 molecules and FP are recorded simultaneously (about 500 oscillations).

Figure 4 shows the transmission spectra of CO_2 molecules at a pressure of 12.16 mbar in cell 3 and FP. Using the HITRAN 2016 spectral database [66], the lines in Fig. 4a have been identified and the frequency scale was determined. After that, the free spectrum range (FSR) was determined from the FP transmission spectrum.
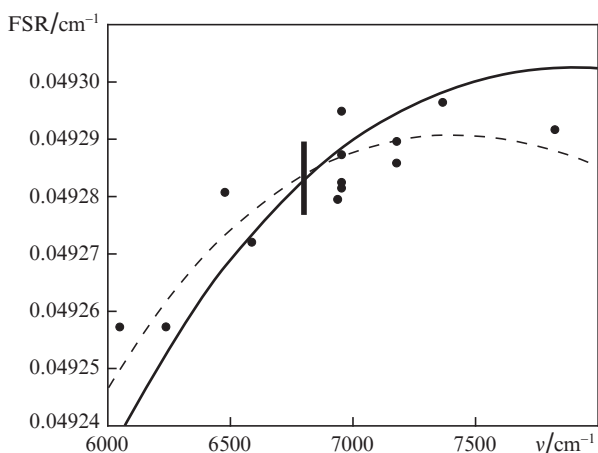

Figure 5. Frequency dependence of the FP free spectrum range: dots are the experimental data, solid curve is the calculation result using (1), dashed curve is the approximation of the experimental data by formula (2). Vertical line shows the measurement error.

Using the above-described procedure and available sets of DLs and molecules, the FP free spectrum range at different frequencies was determined (Fig. 5).

In accordance with the accuracy of HITRAN data, the error in determining the FP free spectrum range should be less than 10^{-4} %; however, a much larger spread is observed in Fig. 5 (~ 0.012 %). This spread is due to the fact that within 25 min, which is the frequency scan time (Fig. 4), a shift of the FP maxima occurs because of a random change in its temperature.

For the operation of our spectrometer, it is required to determine with maximum accuracy the FP free spectrum range for any radiation frequency in the operation range, i.e., it is necessary to obtain an analytical dependence of FSR on frequency. Therefore, we calculated the spectral dependence of the FP free spectrum range with a length $L_{FP} = 6.9380(13)$ cm (this is the measured length of the FP in question) from fused silica using the spectral dependence of the refractive index of fused silica [67]:

$$n = \left[1 + \left(\frac{0.6961663}{\lambda^2 - 0.0684043^2} + \frac{0.4079426}{\lambda^2 - 0.1162414^2} \right. \right.$$
$$\left. \left. + \frac{0.8974794}{\lambda^2 - 9.896161^2} \right) \lambda^2 \right]^{1/2}. \tag{1}$$

This dependence is shown in Fig. 5 (solid curve). One can see a fairly good agreement between the experimental data and

the calculation results. However, to ensure that the calculated curve adequately approximates our experimental data, the curve should be corrected. After a detailed analysis, we obtained a formula for calculating the frequency dependence of the free spectrum range:

$$FSR = \left[\frac{1}{n} \left(1 - \frac{v}{n} \frac{\partial n}{\partial v} \right) \right]_{FS} \frac{1}{2 L_{FP}}$$

$$\times \{ 0.999957(34) - 3.0(7) \times 10^{-7} \text{ cm} \times (v - 7000 \text{ cm}^{-1}) \}, \tag{2}$$

in which, in addition to the dependence of FSR on the FP frequency determined by the dispersion of fused silica, there is a correction factor (in curly brackets). The corresponding dependence calculated by formula (2) is shown in Fig. 5 (dashed curve). Thus, the FP free spectrum range for any frequency from 5500 to 8000 cm^{-1} can be calculated by formula (2) with an accuracy of 0.012 %. This accuracy is a systematic error of frequency measurements using a spectrometer.

3.2. DL operation

The diode laser is excited by trapezoidal periodic pump-current pulses. This leads to periodic scanning of the radiation frequency due to heating of the DL active region by the pump current (Fig. 6) (see [68]). Figure 7 shows the signals that are recorded during the spectrometer operation. Signals from three PDs can be recorded simultaneously (see Fig. 3). In Fig. 7, these are signals from PD1, PD2, and PD3.
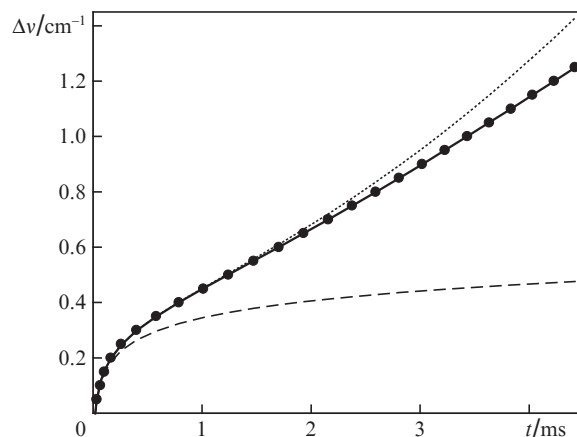

Figure 6. Frequency tuning of DL radiation due to the heating of the active region: dots are the locations of the transmission maxima of the FP transmittance, the dashed curve is the result of two-dimensional temperature diffusion in the DL active region, the dotted curve is the result of heating by the pump current, and the solid curve is frequency tuning due to the establishment of thermal equilibrium in the DL active medium.

The signal at the output of cell 1 is used to stabilise the DL scan cycles (see below). The signals at the FP and RFI outputs are used to calibrate the RFI free spectrum range by the known FP free spectrum range (see Fig. 5). For optimal use of the FP, a plane-parallel radiation beam should be incident on it. This beam, reflecting from the flat surfaces of the etalon, is focused by the lens into the optical fibre, which leads to a strong optical feedback in the DL. For this reason, the FP channel is switched off during the spectrometer operation.
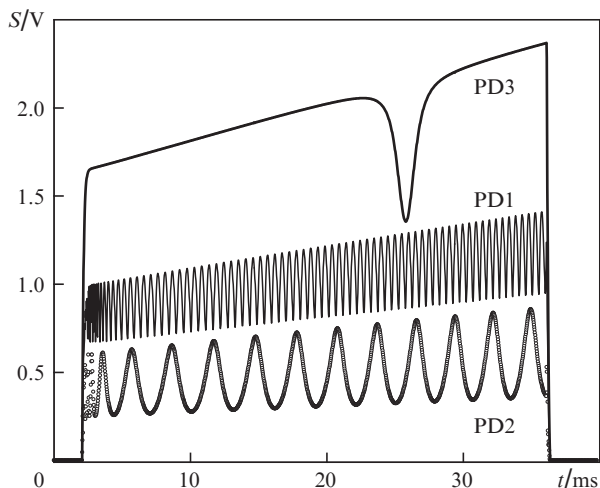
Figure 7. Example of signals recorded during the spectrometer operation.

To calibrate the spectrometer frequency scale, an RFI with a small free spectrum range ($\sim10^{-2}$ cm^{-1}) was used. It was designed on the basis on an X-shaped fibre element. The two ends of this element were connected, resulting in the formation of a high-Q RFI to be used to study the DL lasing spectrum (see below). Frequency calibration requires an RFI with a lower Q-factor, and so a calibrated (10 dB) attenuator was placed between the connected ends of the X-shaped fibre element. From the recorded spectra, the locations of the RFI transmission maxima were determined (Fig. 7). The tuning curve was obtained by spline interpolation.

As many as 10 DL frequency tuning realisations were used to determine the random error of frequency calibration. The standard deviation of the results of these realisations from the mean value was 4.8×10^{-6} cm^{-1}. Thus, the random error of frequency calibration constituted 4.8×10^{-6} cm^{-1}.

3.3. DL lasing spectrum

The DL radiation consists of a narrowband coherent component and broadband spontaneous emission. Therefore, the signal recorded after the passage of radiation through the absorbing medium can be represented as

$$S = S_0(v)\exp[-K(v)L] + \varkappa_{sp}S_0(v). \qquad (3)$$

Here L is the cell length; v is the DL radiation frequency; $K(v)$ is the absorption coefficient of the studied gas; $S_0(v)$ is the signal in the absence of absorption (baseline); and $\varkappa_{sp}$ determines the constant shift of the signal due to spontaneous radiation.

Saturated absorption lines were used to measure the $\varkappa_{sp}$ value. Figure 8 shows an example of water vapour transmission spectra near the 7181.156 cm^{-1} line (cell 3, $P = 0.034-$ 9.705 mbar). One can clearly see that even in the case of a highly saturated line, part of the radiation reaches the PD. This makes it possible to determine the $\varkappa_{sp}$ value, which is usually ~0.001 and varies from laser to laser. We estimate the error of its determination as 0.00016. Based on the known value of $\varkappa_{sp}$, we corrected the absorption coefficient by (3).

A high-Q RFI was used to measure the width of the DL lasing spectrum (see above). Figure 9 shows the signal shape at the output of a high-Q RFI in the regime of a small excess of the DL lasing threshold. This DL lasing threshold (I_{thr}) is
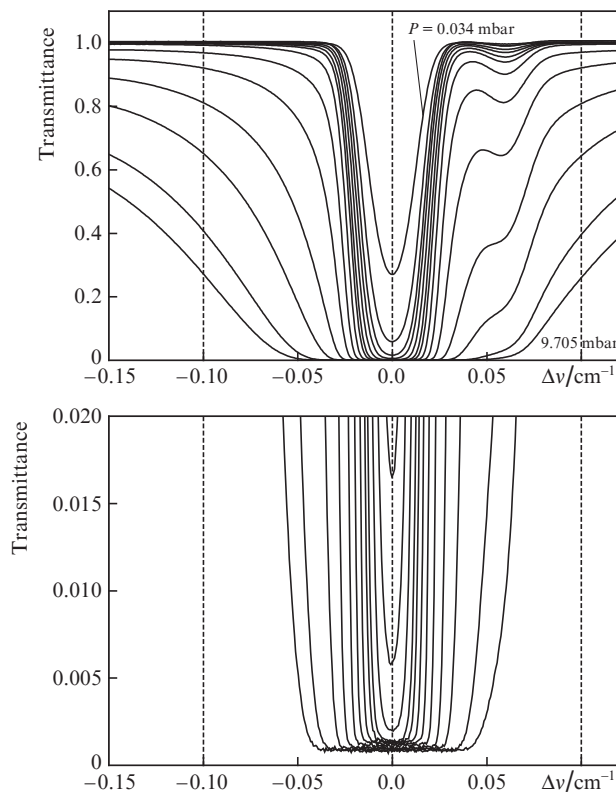

Figure 8. Water vapour transmission spectra near the 7181.156 cm^{-1} line at pressures of 0.034–9.705 mbar and different scales of the ordinate axis.

6.235 mA. When the threshold is exceeded, the signal grows linearly with increasing pump current. The signal is affected by RFI-related features; these features have been used to calibrate the DL radiation frequency.

Figure 10 shows the RFI transmission spectrum for $\Delta v = 0$ at $I = I_{thr}$. This spectrum consists of individual peaks whose amplitude increases and width decreases from left to right. The spectrum in Fig. 10 was approximated by a superposition of Lorentz contours (solid curve). The half-width of an indi-
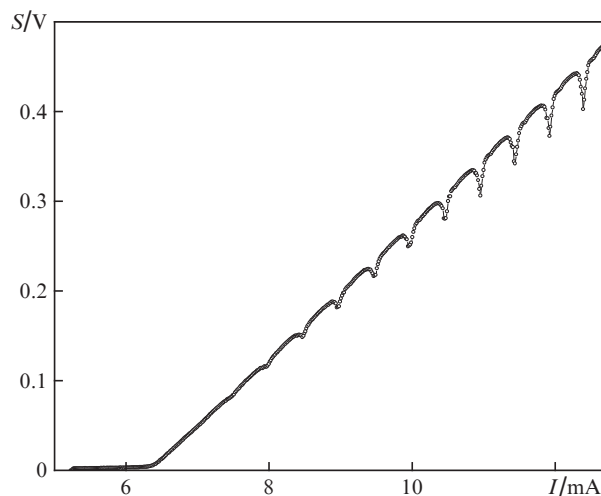

Figure 9. Signal at the RFI output in the regime of a small excess over the DL lasing threshold.

vidual peak was assumed to be equal to the half-width at half maximum (HWHM) of the DL lasing spectrum at the peak of the RFI transmission spectrum. Figure 11 shows the dependence of the DL lasing spectrum half-width on the threshold excess, obtained from the RFI and FP transmission spectra. The half-width is 736 kHz at an operating current of 80 mA.
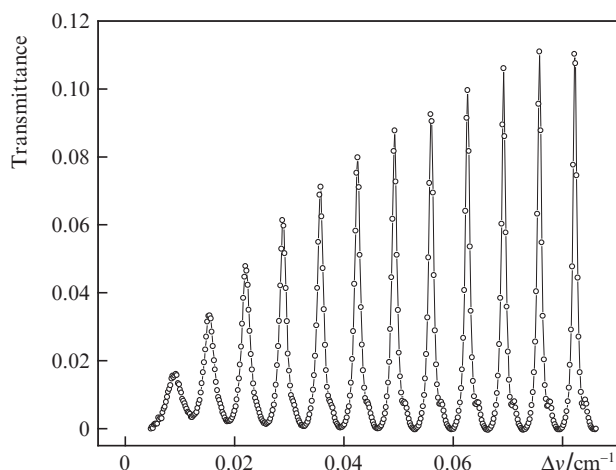

Figure 10. RFI transmission spectrum obtained during the frequency scan cycle of the DL operating in the regime of a small excess over the lasing threshold ($\lambda_0 = 1.39$ μm, $v_0 = 7181.35$ cm^{-1}, $T_0 = 23$ °C).
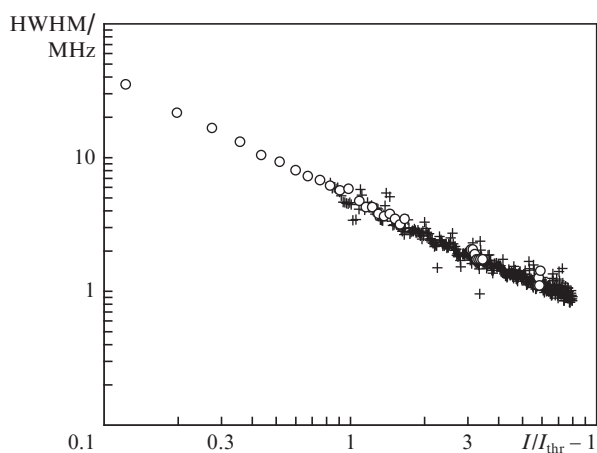

Figure 11. Dependences of the half-width of the DL lasing spectrum on the threshold excess: data were obtained from (○) RFI and (+) FP transmission spectra.

4. Vacuum-gas spectrometer module

The high-precision DL spectrometer includes a vacuum-gas module, the block diagram of which is shown in Fig. 12. The module consists of the three cells discussed above and a set of valves. The connections are made using high-vacuum elements and flexible metal sleeves with flow cross sections of 1/2, 3/4, 1 and 1.5 inches. The module is pre-vacuumed by a fore pump 2. A PFEIFFER turbomolecular pump 1 [69] is used to obtain high vacuum up to 10^{-7} mbar.

The module consists of four stainless steel cylinders. They are alternately cooled in liquid nitrogen and heated to purify
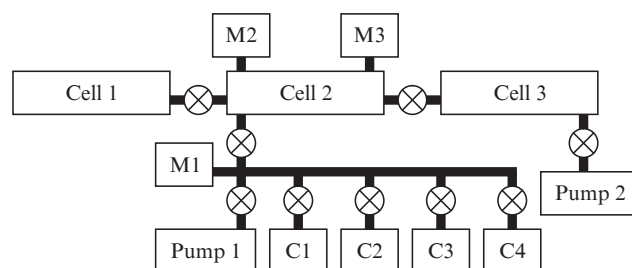

Figure 12. Block diagram of the vacuum-gas module of a high-precision DL spectrometer:
(M1–M3) pressure meters; (C1–C4) cylinders.

the studied gases. They are also used to precisely prepare gas mixtures, to store them, to fill the system with pure gases and mixtures under study, and to pump them out. The ratio of the total module volume to the cylinder volume is 10.4.

4.1. Pressure measurement

The system pressure is controlled by three meters M1, M2, and M3 (Fig. 12).

The M1 meter (EDWARDS WRG (Wide Range Gauge) [70]) is a vacuum gauge in which a Pirani sensor and a reverse magnetron are used as sensors, with a measuring range of 10^{-9}–1000 mbar and low accuracy. This meter is used as a system's vacuum indicator at the level of 10^{-5} mbar.

The M2 meter (Setra model 764) is a capacitive vacuum gauge with a measurement range of 0–1000 Torr and an error of 0.05 Torr [71]. The M2 meter readings are recorded using a TIC measuring instrument controller for vacuum gauges and capacitive pressure gauges [72].

The M3 meter [EDWARDS ASG (Active Strain Gauge), model D357-26-000] is a vacuum gauge in which a strain gauge with the following characteristics is used as a sensor: measurement range, 0–1000 mbar; accuracy and stability, 2 mbar; temperature dependence of the zero drift, 0.5 mbar K^{-1}.

The specified passport accuracy of M1–M3 meters is insufficient for high-precision DLS. Therefore, these meters were additionally calibrated. The M2 meter was tested and calibrated at the ROSTEST Laboratory for verification and testing of pressure and vacuum measurement systems [73]. The calibrated M2 meter was used to calibrate the M3 meter. The systematic measurement error is determined by the calibration accuracy and constitutes 0.014 %; the random error due to the zero drift of the instrument is 0.01 mbar.

4.2. Temperature measurement

The test gas temperature in the spectrometer cells is measured by thermistors [74], and their calibration is performed using a TL-4 No. 879 mercury-glass laboratory thermometer, which was verified and calibrated at the ROSTEST Laboratory for verification and testing of temperature and thermophysical measuring instruments [73]. By using this thermometer, six thermistors mounted in the calibration unit were calibrated. The temperatures measured simultaneously by means of these sensors differed by no more than 0.001 °C. Three calibrated thermistors were installed at the edges and centres of cells 2 and 3. To ensure the temperature uniformity along the cells, they were wrapped with a thick copper wire and placed inside

a duralumin casing. Finally, the entire spectrometer was covered with a thick black cloth to eliminate the effect of temperature nonuniformity in the laboratory room.

The systematic error in measuring the gas temperature is determined by the accuracy of thermistor calibration and constitutes 0.0089 °C. The random error is due to the differences in the readings of different thermistors installed on the same cell. These differences, equal to ∼0.05 °C, are due to the temperature nonuniformity in the laboratory room, caused by various random factors (opening and closing the door, turning on and off the light, etc.).

5. Temperature and frequency stabilisation

Many papers have been published on stabilisation of the radiation frequency of coherent laser sources (see, for example, [75, 76]), in which the stability of the injection laser frequency was determined by the fluctuations in the difference frequency of two independently stabilised lasers. The relative stability attained was $(1.4-4)\times10^{-11}$ at an averaging time of $0.1-10$ s. In our work, the stability of the DL radiation frequency is no worse than 5×10^{-9} during the same times, which fully meets the requirements for high-precision spectroscopy of absorption lines.

5.1. DL temperature and radiation frequency stabilisation

The frequency of DL radiation depends on temperature. Therefore, in a DL spectrometer for high-precision measurements, good DL temperature stabilisation is required. The block diagram of DL temperature stabilisation is shown in Fig. 13.
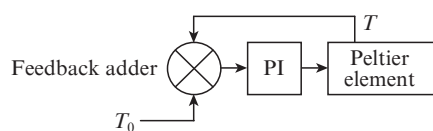

Figure 13. Block diagram of the DL temperature stabilisation: (PI) control unit employing proportional-integral control law; T_0 and T are the set and current temperatures.
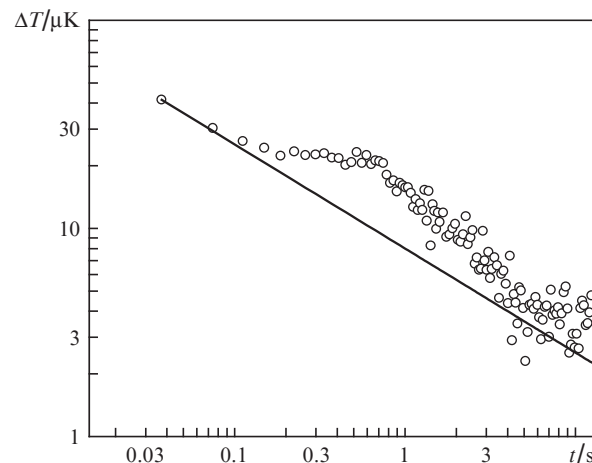

Figure 14. Experimental dependence of the DL temperature instability on (circles) the averaging time and (solid line) white noise of the recording system.
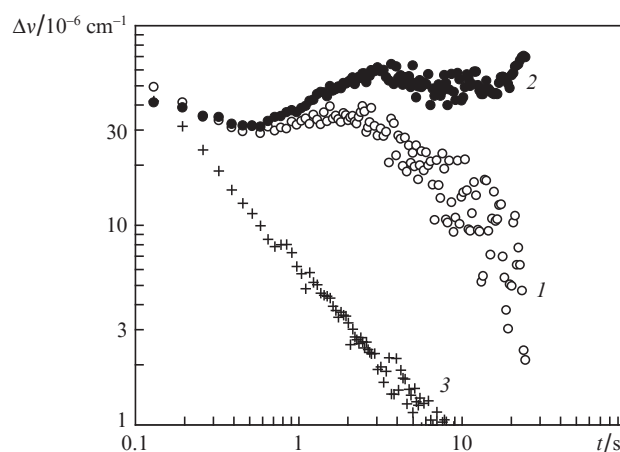

Figure 15. Dependences of the DL radiation frequency instability on the averaging time, obtained using (1) the dependence shown in Fig. 14, (2) the results of measuring the centre frequency of the CO_2 absorption line, and (3) stabilisation of the cycles of scanning the DL radiation frequency.

The DL temperature is measured by a thermistor installed in the DL module. A voltage whose magnitude is proportional to the difference between the measured temperature T and the set temperature T_0 is applied to a Peltier element. The proportional-integral control law is used. Figure 14 shows the Allan plot for the DL temperature, namely the dependence of temperature instability on the averaging time. The oblique line describes the white noise of the recording system.

It is seen that the maximum temperature instability is $25\,\mu K$ in the averaging time range of $0.1-1$ s. The stabilisation accuracy depends on the time constant of the temperature stabilisation system.

5.2. Scan cycle stabilisation

Using the data of Fig. 14 and the coefficient $d\nu/dT = -0.475\,cm^{-1}\,K^{-1}$ that determines the temperature dependence of the given DL frequency, we calculated the dependence of the DL radiation frequency instability on the averaging time [Fig. 15, dependence (1)], which shows that the temperature

stabilisation parameters (Fig. 14) ensure the DL radiation frequency instability at a level not exceeding $3\times10^{-5}\,cm^{-1}$ at the averaging time of $0.1-3$ s, which fully complies with the requirements of high-precision DLS.

Another way to measure frequency instability is to use the absorption line in Fig. 7 (PD3). For each scanning cycle, the frequency of the absorption line centre of CO_2 molecules in cell 1 was measured, and the value $\Delta\nu$ was calculated from these data [Fig. 15, dependence (2)]. Dependence (2) differs significantly from dependence (1); it shows the contribution of flicker noise which is independent of the averaging time, and the contribution of the drift which increases with the averaging time. The difference in dependences (1) and (2) can be understood, since the radiation frequency depends on the temperature of the DL active region, whereas the thermistor-recorded temperature is really stabilised.

To solve this problem, we have proposed a regime to stabilise the DL frequency scan cycles [77], in which the absorption line frequency was measured. The difference between the line frequency and the reference frequency

controlled the DL pump current through the integral control law.

A modern block diagram of the stabilisation of the DL frequency scan cycles is shown in Fig. 16, together with a block diagram of temperature stabilisation. The DL is excited by periodic pump-current pulses, which leads to periodic frequency scanning. The lasing line shift and the DL temperature change are found. Through the integral control law, this change is summed up with T_0. The latest version of the implementation of this scan cycle stabilisation regime is described in [78]. The advantage of this regime is that the possibility of high-precision spectroscopy is combined with the stabilisation of the DL frequency scan cycles. The result of using this regime to stabilise the DL frequency is shown in Fig. 15 [dependence (3)]. One can see a noticeable improvement in frequency stability.
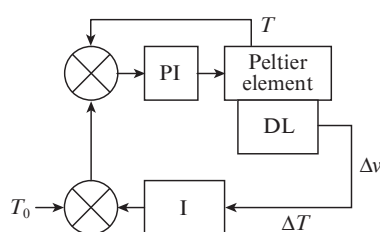

Figure 16. Modern block diagram of stabilisation of the scanning cycles of the DL radiation frequency:
(I) unit employing the integral control law.
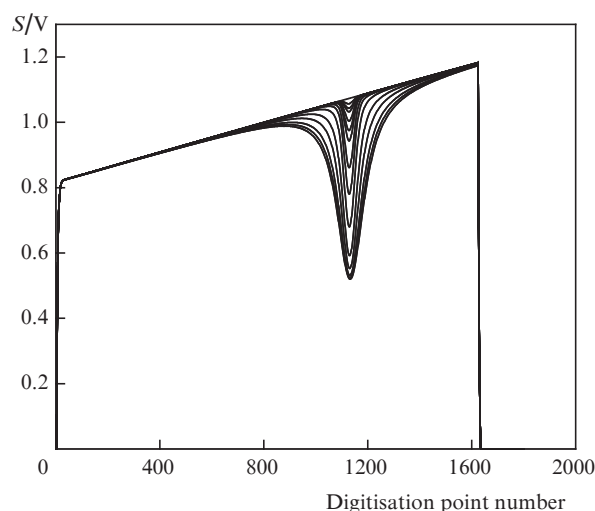
6. Absorption line contour recording

An isolated absorption line was selected for research and testing. This is the P20 line of the $^{12}C^{16}O_2$ molecule (band $00031 - 00001$ according to identification [79], or $3v_3$ according to traditional identification), the frequency of which is 6953.467 cm^{-1} [66].

The following measurement procedure is used. At the start and end of each experiment, the baseline is recorded in the absence of the gas in the cell. Then a series of signals (transmission spectra for the P20 line) is recorded (Fig. 17). Two signals are recorded at each pressure to check the reproducibility of the results. Using (3), the experimental line contour is determined from these signals.

Figure 18 shows the experimentally measured contours of the analytical absorption line at different CO_2 pressures. In this case, the signals at the output of the analytical cell 2 were used. The series of measurements starts with the signal recording after the passage of the analytical cell vacuumed to a pressure of 10^{-6} mbar. This signal (baseline) is stored and then used for normalisation; its recording is repeated 5 times.

The analytical cell 2 is then filled with the gas in question and the signals are recorded after the passage of DL radiation through the cell. Simultaneously with these signals, the readings of the cell temperature and pressure sensors are recorded. Using (3), the absorption contour is found. Figure 18 shows the shock shift and broadening of the absorption line, which increase with pressure.

At the end of the series of measurements, five signals are again recorded for the vacuumed cell, which, together with similar signals recorded at the start of the measurements, are used to determine the baseline.

a
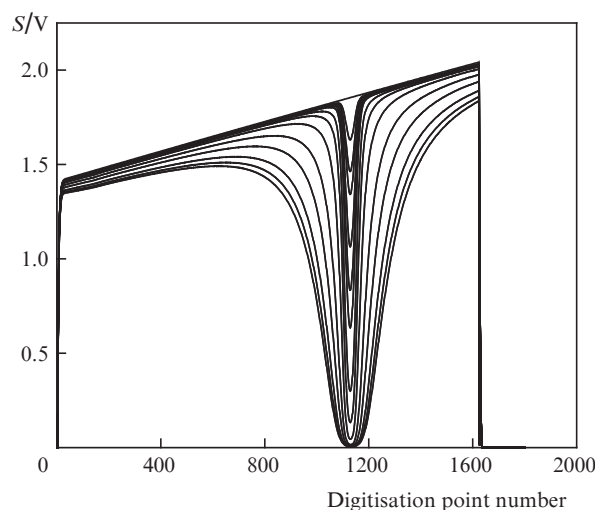
b

Figure 17. CO_2 transmission spectra for the P20 line (a) in cell 2 and (b) in cell 3 at pressures of $3.448 - 236.653$ mbar; $T = 23\,°C$.
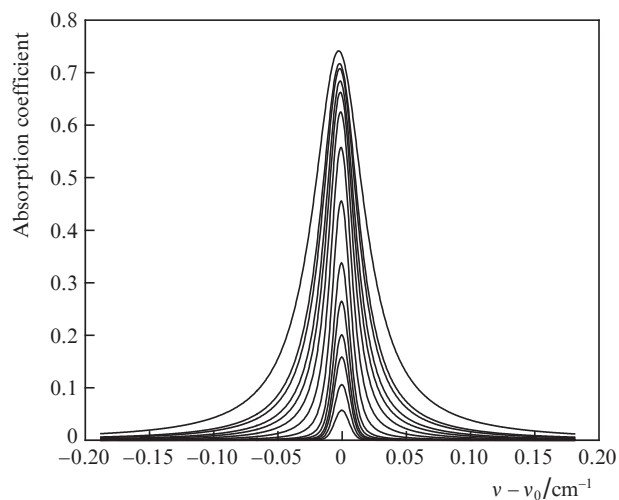

Figure 18. Experimental contours of the analytical absorption line at pressures of $3.448 - 236.653$ mbar.

7. Line contour approximation

To find the absorption line parameters such as the line centre frequency, line intensity, width, etc., the line shape approximation by known model functions is traditionally used [80]. Under some assumptions considered in [80], the spectral line contour represents a convolution of the shock and Doppler contours. The shock contour is described by the Lorentz function:

$$I_v = I(0)\frac{1}{\pi}\frac{\Gamma}{(v-\Delta)^2 + \Gamma^2}, \tag{4}$$

where Γ is the shock width and Δ is the shock shift.

The Doppler contour parameters are determined by solving the kinetic equation with allowance for the collisions of radiating (absorbing) and buffer particles. Two limiting solutions of this equation, corresponding to the models of soft and hard collisions, are found.

The soft collision model assumes that an infinite number of collisions are required for the relaxation of the molecule velocity. An example of the implementation of this model is the scattering of very heavy molecules on very light ones. The soft collision model corresponds to the diffusion approximation in the kinetic equation. It leads to the line shape called the Galatry contour [81]. The hard collision model implies that a single collision is required for molecule velocity relaxation. This contour entered foreign literature under the name of Rautian.

For processing high-precision contours of spectral lines, we have developed an approximation software programme which employs the soft and hard models. As a result of approximation, 6 parameters are determined: y_0 is the baseline level; A is the area occupied by the line; v_0 is the line centre frequency; and L, D, and B are the Lorentz and Doppler widths and the line narrowing ratio, respectively. Figure 19 is an example of the residual in the approximation of an experimental contour by the soft model. It is seen that, at the baseline level of 2.3×10^{-5}, the line contour is well

described by the convolution of Doppler (soft) and shock contours with small asymmetry.

The simplest model of the residual with allowance for asymmetry is presented below:

$$A_{as} = \frac{\partial^2 F}{\partial v^2}(v - v_0) + 0.5\frac{\partial F}{\partial v}, \tag{5}$$

where F is the normalised line contour. Figure 19 shows that the model (line) describes well the experimental contour.

8. Integral line intensity

The intensity of the vibrational–rotational absorption line due to the transition from the state α to the state β of a polyatomic molecule is described by the formula [82]:

$$S_{\alpha\beta} = \frac{8\pi^3}{4\pi\varepsilon_0 3hc} v_{\alpha\beta} \frac{g_a}{Z(T)} \exp\left[-\frac{hcE_\alpha}{kT}\right]$$

$$\times \left[1 - \exp\left(-\frac{hcv_{\alpha\beta}}{kT}\right)\right] R_\alpha^\beta, \tag{6}$$

where $v_{\alpha\beta}$ is the transition frequency; $\alpha > \beta$; k is the Boltzmann constant; g_α is the statistical weight of the level α; E_α is the energy of the lower state; h is the Planck constant; c is the speed of light; $Z(T)$ is the statistical sum; R_α^β is the square of the matrix element module of the transition dipole moment operator; ε_0 is the electric constant; and T is the absolute temperature.

Figure 20 shows the integral intensities of the P20 analytical line of the $00031 - 00001$ band of the CO_2 molecule as a function of pressure in the approximation of line contours by hard and soft models. For an isolated line, the integral intensity must be constant, i.e., independent of pressure. The vertical segment corresponds to a random error (Table 1), which constitutes 0.047% and is determined by the spread of data for different series of experiments. It is seen that the integral intensity is constant with an accuracy of 0.3%. Figure 20 reveals two more subtle effects observed with the available experimental accuracy: a decrease in S_{P20} with increasing
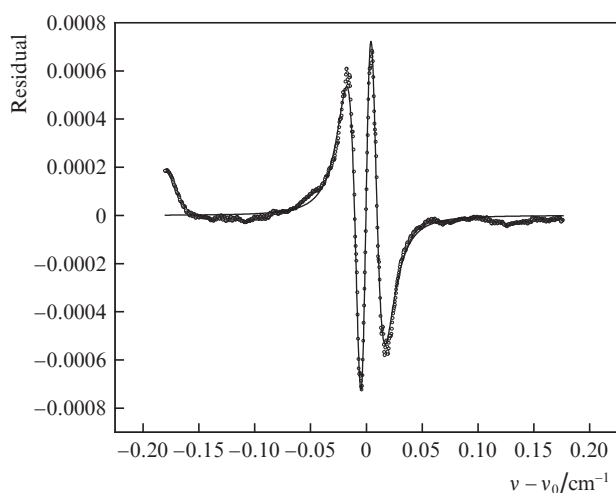

Figure 19. Example of the residuals of the approximation of the experimental absorption line contour: dots are the residual of approximation by the soft model, and the curve is the residual with allowance for asymmetry (5).
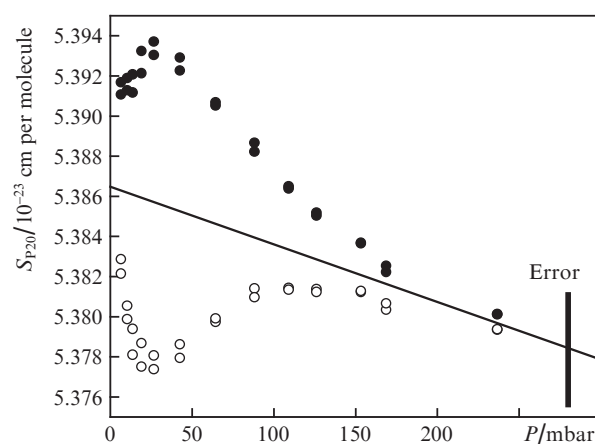

Figure 20. Dependences of integral intensity of the P20 line on the CO_2 pressure in approximating the line contour using (●) hard and (○) soft models, and (solid line) the dependence obtained using the average intensity values corresponding to the two approximation models.

pressure and a difference in the results obtained within the soft and hard models.

The behaviour of the dependence described by the inclined straight line is due to the gas deviation from ideal. The reason for the difference in the results for the soft and hard models is the "statistical dependence of the line broadening due to molecular interaction and the Doppler effect" [80, p. 232].

Table 1 shows the intensity values of the P20 line of the $00031-00001$ band of the CO_2 molecule obtained in this work, and the data from HITRAN and the works of other authors. The accuracy of the line intensity we have measured is significantly higher than the accuracy of the data of other works.

Table 1. Integral intensity of the P20 line of the $00031-00001$ band of the CO_2 molecule.

Year	Intensity/10^{-23} cm per molecule	References
1993	5.32(3)	[83]
2005	5.31(26)	[84]
2006	5.257(54)	[85]
2008	5.267(105)	[86]
2013	5.267(105)	[87]
2017	5.336(53)	[66]
2018	5.3865(85)	This paper

Table 2 demonstrates the accuracy characteristics of the DL spectrometer when measuring the P20 absorption line of the CO_2 molecule.

Table 2. Characteristics of the DL spectrometer in measuring the P20 absorption line of the CO_2 molecule.

Parameter	Value	Random error (%)	Systematic error (%)
Cell length/cm	183.50	0.024	0.022
Temperature range/°C	$20-30$	0.017	0.003
Pressure/mbar	100	0.010	0.014
CO_2 sample purity	0.99998	0.012	0.002
Relative content of the $^{12}C^{16}O_2$ isotopomer	0.98430		0.083
Intermediate total error		0.033	0.087
Photodetector nonlinearity parameter		0.023	0.023
DL radiation frequency stability, $\Delta\nu/10^{-3}$ cm^{-1}	800	0.001	0.001
Relative baseline level (%)	0.003	0.003	0.003
Optical zero level (%)	0.016	0.023	0.026
Lasing line width/kHz	736		0.141
Intermediate total error		0.033	0.145
Total error		0.047	0.169

The random error (precision) is 0.047%, which is orders of magnitude better than the result attained to date worldwide. The total systematic error (accuracy) was calculated as the square root of a sum of the squares of systematic errors arising when individual parameters are taken into account. It constitutes 0.17%.

9. Conclusions

A diode laser spectrometer for high-precision measurements has been developed, calibrated, and put into operation. For tests and measurements, an isolated P20 line of the $00031-$

00001 band of the $^{12}C^{16}O_2$ molecule has been selected. The spectrometer error budget has been analysed. Random and systematic errors constitute 0.047% and 0.17%, respectively, and are due to the uncertainty of the sample's isotopic composition and the lasing spectrum width of the diode laser. A software programme for the approximation of analytical spectral lines using models of soft and hard collisions has been designed [80]. The approximation procedure has been analysed. It is shown that for the baseline level of 2.3×10^{-5}, when approximating the absorption line contour, it is sufficient to use six fitting parameters. The integral intensity value of the analytical line has been measured, amounting to $5.3865(85) \times 10^{-23}$ cm per molecule. The obtained result is compared with the literature data. The integral intensity is independent of the CO_2 pressure with an accuracy of 0.3%. Within the limits of experimental accuracy, two subtle effects have been revealed: The deviation of gas from ideality and the correlation of phase changes in molecular oscillation and molecule velocity at collisions [80, p. 232].

References

1. Basov N.G., Vul B.M., Popov Yu.M. *Sov. Phys. JETP*, **10**, 416 (1960) [*Zh. Eksp. Teor. Fiz.*, **37**, 587 (1960)].
2. Basov N.G., Krokhin O.N., Popov Yu.M. *Sov. Phys. JETP*, **13**, 1320 (1961) [*Zh. Eksp. Teor. Fiz.*, **40**, 1879 (1961)].
3. Basov N.G. *Usp. Fiz. Nauk*, **85**, 585 (1965).
4. Nasledov D.N., Rogachev A.A., Ryvkin S.M., Tsarenkov B.V. *Sov. Phys. Solid State*, **4**, 2449 (1962) [*Fiz. Tverd. Tela*, **4**, 1062 (1962)].
5. Hall R.H., Fenner G.E., Kingsley J.D., Soltys T.J., Carlson R.O. *Phys. Rev. Lett.*, **9**, 366 (1962).
6. Butler J.F., Calawa A.R., Phelan R.J., Strauss A.J., Harmann T.C., Redicker R.H. *Appl. Phys. Lett.*, **5**, 75 (1964).
7. Hinkley E.D. *Appl. Phys. Lett.*, **16**, 351 (1970).
8. http://tdls.gpi.ru/history.html.
9. Mantz A.W., Nadezhdinskii A.I. (Guest Eds) *Spectrochim. Acta, Part A*, **52** (7) (1996).
10. Mantz A.W., Nadezhdinskii A.I. (Guest Eds) *Spectrochim. Acta, Part A*, **55** (10) (1999).
11. Mantz A.W., Nadezhdinskii A.I. (Guest Eds) *Spectrochim. Acta, Part A*, **58** (9) (2002).
12. Mantz A.W. (Guest Ed.) *Spectrochim. Acta, Part A*, **60** (14) (2004).
13. Mantz A.W. (Guest Ed.) *Spectrochim. Acta, Part A*, **63** (5) (2006).
14. Richter D., Fried A., Tittel F. (Guest Eds) *Appl. Phys. B*, **90** (2) (2008).
15. Sigrist M.W., Tittel F.K. (Guest Eds) *Appl. Phys. B*, **100** (2) (2010).
16. Wysocki G., Orr-Ewing A. (Guest Eds) *Appl. Phys. B*, **109** (3) (2012).
17. Tittel F.K. et al., in *Topics in Applied Physics* (Springer, 2003) Vol. 89, pp 445 – 510.
18. Zasavitskii I.I. *Zarubezhn. Elektron.*, (10), 74 (1974).
19. Hinkley E., Ku R., Kelley E., in *Laser Monitoring of Atmosphere*. Ed. by E.Hinkley (Berlin: Springer-Verlag, 1976) p. 237.
20. Nill K.W. *Laser Focus*, **13**, 32 (1977).
21. Hinckley E.D., Nill K.V., Blum V.A., in *Laser Spectroscopy of Atoms and Molecules* (Berlin, Heidelberg: Springer, 1976; Moscow: Mir, 1979).
22. Butler J.E., Nill K.W., Mantz A.W. *Proc. SPIE*, **158** (1978).
23. Eng R.S., Butler J.E., Linden K.J. *Opt. Eng.*, **19**, 945 (1980).
24. McDowell R.S., in *Vibrational Spectra and Structure* (New York: Elsevier, 1981).
25. Eng R., Ku R.T. *Spectr. Lett.*, **15**, 803 (1982).
26. Kosichkin Yu.V., Nadezhdinskii A.I. *Strukt. Khim.*, **24**, 114 (1983).
27. Kuritsyn Yu.A., in *Lazernaya analiticheskaya spektroskopiya* (Laser Analytical Spectroscopy). Ed. by V.V. Letokhov (Moscow: Nauka, 1986) p. 120.

28. Nadezhdinskii A., Prokhorov A. *Proc. SPIE*, **1724** (1992), https://doi.org/10.1117/12.140314.
29. Niemax K. *Spectrochim. Acta Rev.*, **15**, 289 (1993).
30. Werle P. *Spectrochim. Acta, Part A*, **54**, 197 (1998).
31. *Proc. SPIE*, **438** (1983).
32. Grisar R., Preier H., Schmidtke G., Restelli G. (Eds) *Proc. Int. Symposium, Freiburg, FRG 1986* (Dordrecht: D.Reidel Publ. Com., 1987).
33. Grisar R., Schmidtke G., Tacke M., Restelli G. (Eds) *Proc. Int. Symposium, Freiburg, FRG 1988* (Dordrecht: Kluwer Acad. Publ., 1989).
34. Grisar R., Bottner H., Tacke M., Restelli G. (Eds) *Proc. Int. Symposium, Freiburg, Germany, 1991* (Dordrecht: Kluwer Acad. Publ., 1992).
35. *Infrared Phys. Technol.*, **37** (1) (1996).
36. Fried A. (Ed.) *Proc. SPIE*, **2834** (1996).
37. Allan D.W. *Proc. IEEE*, **54**, 221 (1966).
38. http://www.dls.gpi.ru/rus/conf/TDLS2009/Posters/B1_Fundamental noises in TDLS.pdf.
39. Werle P., Lechner S. *Spectrochim. Acta, Part A*, **55**, 1941 (1999).
40. McManus J., Zahniser M., Nelson D., Williams L., Kolb C. *Spectrochim. Acta, Part A*, **60**, 3325 (2002).
41. Wirtz D., Sonnabend G., Schieder R. *Spectrochim. Acta, Part A*, **58**, 2457 (2002).
42. Richter D., Fried A., Wert B.P., Walega J.G., Tittel F.K. *Appl. Phys. B*, **75**, 281 (2002).
43. Kormann R., Fischer H., Klupfel Th., Kowalski K., Koningstedt R., Parchatka U., Vagner V. *Spectrochim. Acta*, **58**, 2489 (2002).
44. Wert B., Fried A., Rauenbuehler S., Walega J., Henry B. *J. Geophys. Res.*, **108** (D12), 4530 (2003).
45. Durry G., Pouchet I., Amarouche N., Danguy T., Megie G. *Appl. Opt.*, **39**, 5609 (2000).
46. Ikegami T., Sudo S., Sakai Y. *Frequency Stabilization of Semiconductor Laser Diodes* (Norwood, MA: Artech House, Inc., 1995) p. 64.
47. Bakhirkin Yu., Kosterev A., Roller C., Curl R., Tittel F. *Appl. Opt.*, **43**, 2257 (2004).
48. Sonnenfroh D., Allen M. *Appl. Opt.*, **35**, 4053 (1996).
49. Gustafsson U., Somesfalean G., Alnis J., Svanberg S. *Appl. Opt.*, **39**, 3774 (2000).
50. Werle P., Popov A. *Appl. Opt.*, **38**, 1494 (1999).
51. Kim J., Yoo Y., Lee J.Y., Lee J.B., Hahn J. *Appl. Opt.*, **40**, 5509 (2001).
52. Kosterev A., Malinovsky A., Tittel F., Gmachl C., Capasso F., Sivco D., Baillargeon J., Hutchinson A., Cho A. *Appl. Opt.*, **40**, 5522 (2001).
53. Wysocki G., Bakhirkin Yu., So S., Tittel F., Hill C., Yang R., Fraser M. *Appl. Opt.*, **46**, 8202 (2007).
54. Liger V.V., Kuritsyn Yu.A., Krivtsun V.M., Snegirev E.P., Kononov A.N. *Quantum Electron.*, **27**, 360 (1997) [*Kvantovaya Elektron.*, **24**, 371 (1997)].
55. Liger V., Zybin A., Kuritsyn Yu., Niemax K. *Spectrochim. Acta, Part B*, **52**, 1125 (1997).
56. http://www.dls.gpi.ru/rus/conf/TDLS2009/Posters/C1_Flicker.pdf.
57. http://www.dls.gpi.ru/rus/conf/TDLS2009/Posters/D1_Baseline.pdf.
58. Nadezhdinskii A.I., Ponurovskii Ya.Ya. *Zh. Analit. Khim.*, **73**, 153 (2018).
59. http://www.gosthelp.ru/gost/gost5270.html.
60. http://vsegost.com/Catalog/28/28590.shtml.
61. http://www.ntt-electronics.com/.
62. http://www.anritsu.co.jp/.
63. http://www.fitel.com/index_nf.htm.
64. http://www.eblanaphotonics.com/.
65. http://www.lasercomponents.com/.
66. Gordon I.E., Rothman L.S., et al. *J. Quantum Spectrosc. Radiat. Transfer*, **203**, 3 (2017).
67. Malitson I.H. *J. Opt. Soc. Am.*, **55** (10), 1205 (1965).
68. Nadezhdinskii A. *Spectrochim. Acta, Part A*, **52**, 959 (1996).
69. http://amnol.usv.ro/DOC/Pfeiffer_HiCube80_Eco.pdf.
70. http://www.shop.edwardsvacuum.com/products/r60/list.aspx.
71. http://www.setra.com/products/obsolete/model-764/.
72. http://images.iop.org/cws/cms/phw/microsites/A100006265/ images/ 9_TIC_Instrument_Controller.pdf.
73. http://www.rostest.ru/.
74. http://www.teamwavelength.com.
75. Akul'shin A.M., Velichanskii V.L., Zibrov A.S., Nikitin V.V., Sautenkov V.A., Kharisov G.G. *Sov. J. Quantum Electron.*, **18**, 1214 (1988) [*Kvantovaya Elektron.*, **15**, 1945 (1988)].
76. Velichansky V.L., Gubin M.A. *Usp. Fiz. Nauk*, **179**, 1219 (2009).
77. Kosichkin Yu.V., Kuznetsov A.I., Nadezhdinskii A.I., Perov A.N., Stepanov E.V. *Sov. J. Quantum Electron.*, **12**, 518 (1982) [*Kvantovaya Elektron.*, **9**, 822 (1982)].
78. http://www.dls.gpi.ru/rus/conf/TDLS2005/Posters/B10.pdf.
79. Rothman L., Young L. *J. Quantum Spectrosc. Radiat. Transfer*, **25**, 505 (1981).
80. Rautian S.G., Sobel'man I.I. *Usp. Fiz. Nauk*, **90**, 209 (1966).
81. Galatry L. *Phys. Rev.*, **122**, 1218 (1961).
82. Flaud J.M., Cay-Peyret C. *J. Mol. Spectrosc.*, **55**, 278 (1975).
83. Johns J.W.C., Lu Z., Thibault F., Le Doucen R., Arcas P., Boulet C. *J. Mol. Spectrosc.*, **159**, 259 (1993).
84. Rothman L.S., Jacquemart D., Barbe A., et al. *J. Quantum Spectrosc. Radiat. Transfer*, **96**, 139 (2005).
85. Toth R.A., Brown L.R., Miller C.E., Devi V., Chris Benner D. *J. Mol. Spectrosc.*, **239**, 221 (2006).
86. Toth R.A., Brown L.R., Miller C.E., Malathy Devi V., Benner D. *J. Quantum Spectrosc. Radiat. Transfer*, **109**, 906 (2008).
87. Rothman L.S., Gordon I.E., Babikov I., Barbe A., et al. *J. Quantum Spectrosc. Radiat. Transfer*, **130**, 4 (2013).